ADVANCED FUNCTIONAL MATERIALS
www.afm-journal.de

GeO_x/Reduced Graphene Oxide Composite as an Anode for Li-Ion Batteries: Enhanced Capacity via Reversible Utilization of Li_2O along with Improved Rate Performance

*Dongping Lv, Mikhail L. Gordin, Ran Yi, Terrence Xu, Jiangxuan Song, Ying-Bing Jiang, Daiwon Choi, and Donghai Wang**

A self-assembled GeO_x/reduced graphene oxide (GeO_x/RGO) composite, where GeOx nanoparticles are grown directly on reduced graphene oxide sheets, is synthesized via a facile one-step reduction approach and studied by X-ray diffraction, transmission electron microscopy, energy dispersive X-ray spectroscopy, electron energy loss spectroscopy elemental mapping, and other techniques. Electrochemical evaluation indicates that incorporation of reduced graphene oxide enhances both the rate capability and reversible capacity of GeO_x, with the latter being due to the RGO enabling reversible utilization of Li_2O. The composite delivers a high reversible capacity of 1600 mAh g^{-1} at a current density of 100 mA g^{-1}, and still maintains a capacity of 410 mAh g^{-1} at a high current density of 20 A g^{-1}. Owing to the flexible reduced graphene oxide sheets enwrapping the GeO_x particles, the cycling stability of the composite is also improved significantly. To further demonstrate its feasibility in practical applications, the synthesized GeO_x/RGO composite anode is successfully paired with a high voltage $LiNi_{0.5}Mn_{1.5}O_4$ cathode to form a full cell, which shows good cycling and rate performance.

1. Introduction

High energy/power Li-ion batteries have been attracting great attention recently due to the increasing demand for advanced energy storage techniques, especially with the emergence of electric vehicles (EV) and hybrid electric vehicles (HEV).[1,2] Anode materials with high specific capacity and rate capability are one of the key components of such batteries. Traditional carbon-based anode materials exhibit acceptable overall performance with respect to the energy/power requirements of existing portable electronic devices, but have a relatively low specific capacity, poor Li^+ insertion/extraction kinetics, and documented safety issues.[3] These downsides make carbon-based anodes inadequate for many upcoming applications and have impelled researchers to find alternative high-capacity anode materials, for example, Si, Ge, and metal oxides.[4–7] Though not yet heavily investigated compared with silicon, germanium has a high capacity of 1600 mAh g^{-1}, four times higher than that of commercial graphite, plus a four orders of magnitude higher intrinsic electronic conductivity and 400 times higher Li-ion diffusivity than Si.[8] In spite of its relatively high cost, these qualities make Ge an attractive anode candidate for high-power Li-ion batteries. The core challenge of Ge anodes is similar to that of Si anodes: crystalline Ge undergoes large volume change upon Li^+ insertion/extraction, leading to pulverization and loss of electrical contact within an electrode and thus to capacity fading. Attempts have been made to address these issues with incremental improvements by using structured nanoscale morphologies to mitigate fracture and pulverization of Ge[9–13] and developing carbon-based nanocomposites to improve electrical contact after pulverization.[14–16] Recently, it was found that nanosized germanium-based oxides show significantly better cycling stability than pure Ge, demonstrating the potential of germanium-based anode materials in advanced Li-ion batteries.[17–19] Even so, relatively low conductivity is anticipated from such oxides. As lithiation of germanium oxides involves the formation of Ge and Li_2O,[17] achieving a high reversible capacity involves the kinetically slow reaction of Li_2O with Ge metal during delithiation, which is still a challenge especially at high current rates.

Incorporating conductive additives to form composites has been demonstrated as an efficient approach to improving electron transport and maintaining electrical contact in electrodes and thus improving the high-rate performance and cycling stability of high-volume-change anodes such as Si and Ge.[5,20–22] Owing to their excellent electronic conductivity and high specific surface area,[23,24] incorporation of graphene or reduced

Dr. D. P. Lv, M. L. Gordin, R. Yi, T. Xu, Dr. J. X. Song, Dr. D. H. Wang
Department of Mechanical & Nuclear Engineering
the Pennsylvania State University
University Park, PA, 16802, USA
E-mail: dwang@psu.edu
Dr. Y.-B. Jiang
Center for Micro-Engineered Materials
University of New Mexico
Albuquerque, NM, 87131, USA
Dr. D. Choi
Energy and Environment Directorate
Pacific Northwest National Laboratory
Richland, WA, 99354, USA

DOI: 10.1002/adfm.201301882

graphene oxide sheets to form composites has been widely studied to enhance the electrochemical performance of electrode materials. Graphene sheets can improve electron transport and thus enhance the rate performance of electrode materials, including metal oxides, intermetallic alloys (such as Si and Ge), polymers, and polyanionic oxides.[7,14,25–33] Additionally, graphene sheets can also direct self-assembly of active electrode materials into structured composites and thereby improve their cycling stability. For example, graphene sheets have been observed to anchor nanoparticles of large-volume-change anode materials (such as SnO_2 and Si), helping them to maintain electrical contact during cycling and leading to improved cycling stability.[28,34,35]

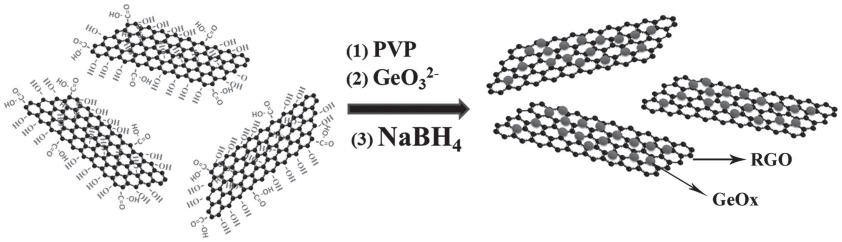

Scheme 1. One-step reduction synthesis of GeO_x/RGO nanocomposites.

Herein, we report a composite of nano-sized GeO_x and reduced graphene oxide sheets (GeO_x/RGO) as a Li-ion battery anode. Importantly, we demonstrate a new finding regarding the use of reduced graphene oxide in composite materials for energy storage: its ability to promote reversible utilization of Li_2O. Li-ion storage by conversion reaction of oxide materials with Li ions has been reported for decades.[36] However, irreversible generation of Li_2O is a limitation for most oxide anodes. We found that reversible utilization of Li_2O in the GeO_x/RGO composite was due to formation of nanostructures of GeO_x in intimate contact with graphene sheets. In addition, we also found the GeO_x/RGO composite anode to have enhanced rate performance. To demonstrate the GeO_x/RGO composite's viability for practical applications, we assembled a full cell using the composite anode paired with a $LiNi_{0.5}Mn_{1.5}O_4$ cathode and found that it had good rate performance and cycling stability.

2. Result and Discussion

Our previous studies indicate that it is important to disperse graphene well in graphene-based composites in order to enhance their electrochemical performance, because the well-dispersed graphene can increase electrical contact area and improve electrical conductivity. One of the crucial steps during synthesis of the composites is obtaining a homogeneous and stable solution composed of graphene and other precursors.[25,35,37,38] Many approaches have been adopted to increase dispersibility of graphene in precursor solution, for example, using dispersing agents such as surfactants, polymers, or aromatic molecules, or choosing graphene oxide as a precursor due to its good dispersibility in aqueous solution. The rich surface functional groups of graphene oxide can also provide preferred nucleation sites for the growth of metal oxides, further helping to achieve good dispersion in the final composite. In the present work, graphene oxide and the surfactant poly(vinylpyrrolidone) (PVP) were utilized to achieve good dispersion, promote nucleation of germanium oxide on graphene oxide, and confine the growth of germanium oxide into nanoparticles. As shown in **Scheme 1**, graphene oxide was firstly dispersed in water to form a uniform dispersion. PVP was then added and dissolved by ultrasonication. GeO_3^{2-} precursor solution, obtained through direct reaction of GeO_2 and NH_4OH aqueous solution, was added drop-wise into the GO/PVP dispersion under ultrasonication. As a result, a homogeneous precursor dispersion containing the GO, PVP, and GeO_3^{2-} was obtained. Addition of reducing $NaBH_4$ solution caused the yellowish GO/PVP/GeO_3^{2-} dispersion to gradually turn to black, indicating the transformation of GO into RGO sheets. With continued addition of $NaBH_4$ solution, a suspension containing brownish-red particles was obtained. This was ascribed to the formation of GeO_x through in situ reduction of GeO_3^{2-} by $NaBH_4$.[20] Due to PVP serving as a capping ligand in assisting the formation of nanoparticles, GeO_x were grown into nanosized particles, which were anchored onto reduced graphene oxide sheets.[15,39]

The GeO_x/RGO composite was first investigated by X-ray diffraction (XRD). As shown in **Figure 1**a, the composite exhibits an amorphous structure, with only one broad diffraction peak observed at 2θ of 20–35°. The characteristic broad peak is ascribed to the diffraction of short-range ordered Ge–O crystalline structure in amorphous GeO_x,[40] and indicates the nanosized particles of the materials. If heated at 600 °C under Ar, the GeO_x in the composite disproportionates and phase separates into crystalline GeO_2 and Ge (Figure S1b, Supporting Information), as confirmed by comparison with the standard XRD patterns shown in Figure S1c,d (Supporting Information, JCPDS no. 65–8052 and 65–0333, respectively). This demonstrates that the germanium oxide species in the composite was GeO_x where $x < 2$ instead of pure GeO_2 or Ge, with the value of x determined as described below.[40,41] The presence of the Ge–O bond in GeO_x was further proved by Fourier transform infrared spectroscopy (FTIR). As shown in Figure S2a (Supporting Information), absorbance observed at 860 cm^{-1} is ascribed to the characteristic stretching vibration of the Ge–O bond.[42] To determine the content of oxygen in the GeO_x/RGO composite, thermogravimetric analysis-mass spectrometry (TG-MS) and elemental analysis were also carried out. The TG profile (Figure S2b, Supporting Information) shows distinct weight loss steps at temperatures of 120 °C and 420 °C. Based on MS analysis, these two weight losses are ascribed to the removal of physically adsorbed water and dehydration of OH^- in the composite. As a result, the total fraction of H_2O in the composite was found to be around 9.5 wt%. Combining this with elemental analysis of C and O (Table S1, Supporting Information), the composition of the composite is determined to be GeO_x/RGO ($1.01 < x < 1.07$) (see Supporting Information) considering the measured carbon content of 8.5 wt% and that the C/O ratio of RGO is in the range of 5–8 when $NaBH_4$ is used as the reducing agent.[43,44]

The structure of the self-assembled GeO_x/RGO composite was further investigated by transmission electron microscopy

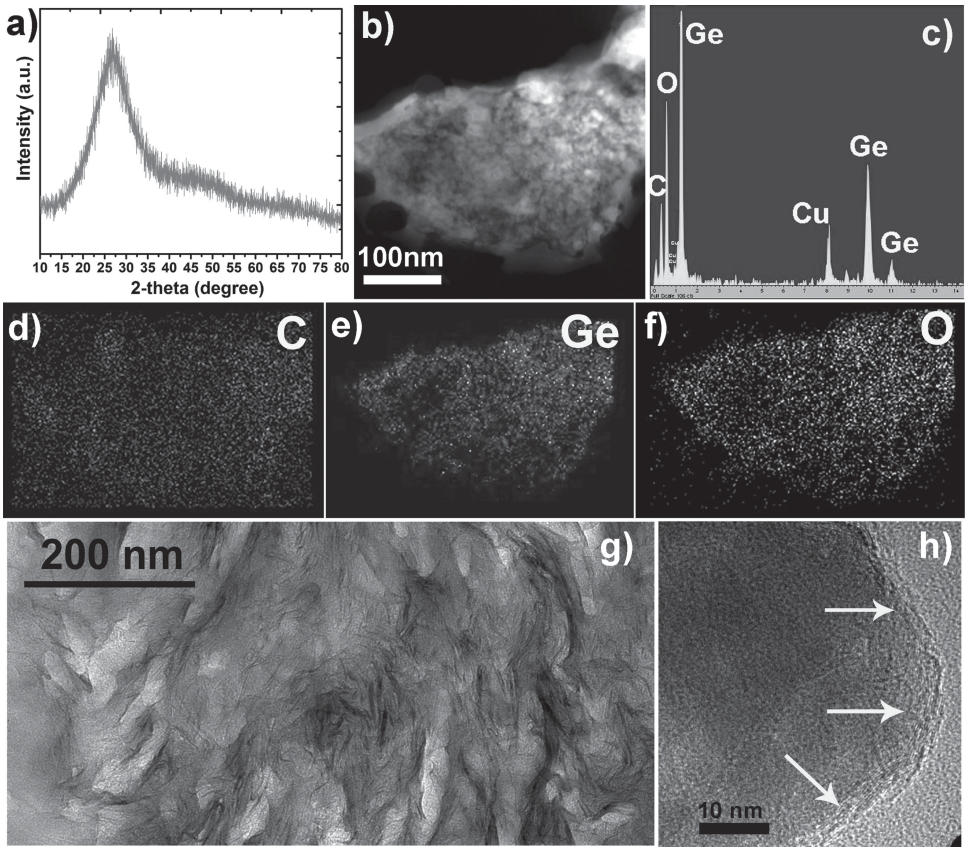

Figure 1. Morphology and structural characterization of a GeO_x/RGO composite. a) XRD pattern, b) dark field TEM image, c) EDS spectrum, d–f) corresponding EELS elemental mapping images of d) carbon, e) germanium, and f) oxygen in the composite in (b), g) cross-section TEM image, and h) high resolution TEM image (arrows point to the RGO layers).

(TEM). TEM images of the GeO_x/RGO composite (Figure 1b and Figure S3, Supporting Information) show that GeO_x nanoparticles aggregate and are anchored on reduced graphene oxide sheets. The primary particle size is in the range of 20–40 nm (Figure S3b, Supporting Information), which is consistent with the single broad peak observed in the XRD pattern (Figure 1a). Energy-dispersive X-ray spectroscopy (EDS) confirms the presence of carbon, germanium, and oxygen in the GeO_x/RGO composite (Figure 1c). The corresponding electron energy loss spectroscopy (EELS) elemental mapping images show uniformly-distributed C, Ge, and O in the composite (Figure 1d–f, respectively), indicating uniform distribution of GeO_x on the RGO sheet. This indicates that the GeO_x could be grown on the RGO sheet via the in situ reduction and self-assembly process. The distribution of GeO_x within the composite was further studied by cross-section TEM (Figure 1g), which shows RGO sheets intertwined with amorphous GeO_x and dispersed across the composite. High-resolution TEM (HRTEM) further demonstrates that GeO_x particles are in intimate contact with reduced graphene oxide sheets. Some multi-layered reduced graphene oxide sheets (about 3–5 layers) were observed due to stacking of single sheets of reduced graphene oxide (Figure 1h).

To determine whether the incorporation of the RGO sheets improved the electrochemical properties of GeO_x, galvanostatic charge–discharge tests were carried out at various current densities. **Figure 2**a shows the first three charge–discharge curves of the GeO_x/RGO composite at a low current density of 100 mA g^{-1}. A high discharge capacity of approximately 2200 mAh g^{-1} (based on the mass of GeO_x) was achieved in the

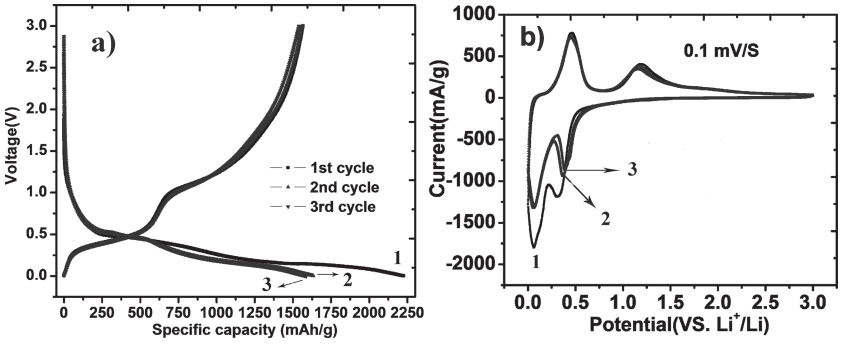

Figure 2. a) The first three charge/discharge profiles of GeO_x/RGO at a current density of 100 mA g^{-1} between 0.01 and 3 V, and b) the first three cyclic voltammetry curves of GeO_x/RGO at a scan rate of 0.1 mV s^{-1} between 0.01 and 3 V.

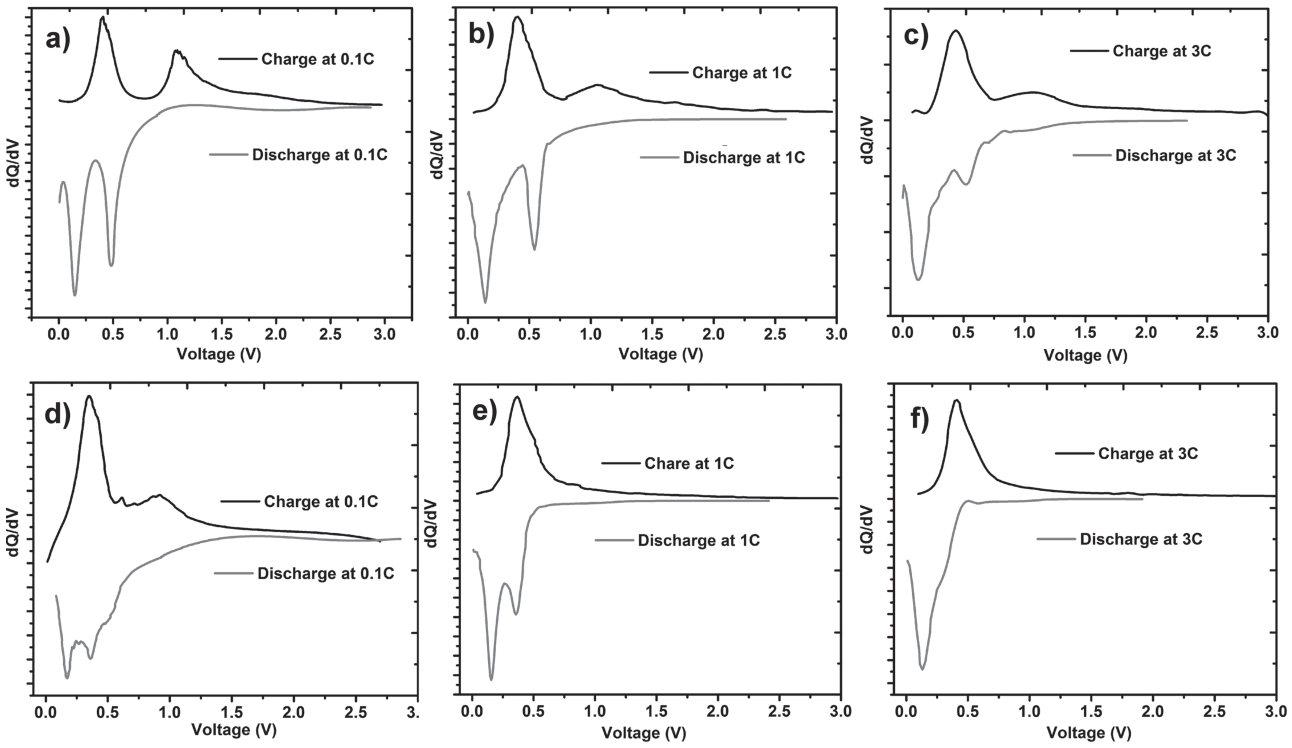

Figure 3. The differential capacity (d*Q*/d*V*) curves of the GeO_x/RGO composite cycled at a) 0.1 C, b) 1 C, and c) 3 C, and comparison with those of as-synthesized GeO_x at d) 0.1 C, e) 1 C, and f) 3 C.

first cycle. The reversible capacity of the pure RGO used in the composite was measured to be around 250 mAh g^{-1} (Figure S4, Supporting Information), so capacity contributed to the composite by the RGO was only 20 mAh g^{-1} considering the carbon content of 8.5 wt% in the composite. The first discharge specific capacity exceeds the theoretical capacity of GeO_x (1938–1954 mAh g^{-1} depending on x, where $1.01 < x < 1.07$) due to the formation of a solid electrolyte interphase (SEI) layer on the surface of GeO_x/RGO.[9,16] During the subsequent cycles, a stable reversible capacity of 1600 mAh g^{-1} and a charge–discharge efficiency of over 97% were obtained. Besides SEI formation,[14,45] the capacity difference between the first and subsequent discharge processes is also partially ascribed to the incomplete conversion of Li_2O during delithiation of lithiated RGO[46] and lithiated GeO_x[17] during the first charge process. Electrochemical lithiation of GeO_x usually involves irreversible conversion of GeO_x to Ge and Li_2O followed by subsequent alloying of Ge with Li reversibly to form $Li_{4.4}Ge$. The reversible alloying and de-alloying between Ge and $Li_{4.4}Ge$ take place at about 0.10 and 0.50 V in the discharge and charge processes, respectively.[12,47] An additional discharge plateau at 0.45 V and charge plateau at 1.1 V were observed in cycling of the GeO_x/RGO, which can be attributed to the reversible conversion between Li/GeO_x and Li_2O/Ge. This indicates the formed Li_2O can be partially activated and cycled reversibly in the GeO_x/RGO composite at a relatively low current density (100 mA g^{-1}) during the charge/discharge processes, which was also observed by Wang et al.[17] Based on the observed stable reversible capacity of 1600 mAh g^{-1} at 100 mA g^{-1}, and theoretical capacity of 1938–1954 mAh g^{-1} in GeO_x (estimated 6.42–6.54 Li^+ per formula with respect to x between 1.01 and 1.07), it is estimated that 5.30–5.35 mol Li^+ per formula unit can be reversibly stored and released in the system, indicating 44.4–44.6% of Li_2O was reversibly utilized (see Supporting Information). The electrochemical lithiation/delithiation profiles of the GeO_x/RGO composite are consistent with cyclic voltammetry (CV) analysis (Figure 2b). Two cathodic peaks were observed in the first negative CV scan at voltages of 0.31 and 0.06 V, which are ascribed to the electrochemical conversion of GeO_x to Ge and alloying process of Ge to $Li_{4.4}Ge$, respectively. In the first positive CV scan, de-alloying of $Li_{4.4}Ge$ occurred at 0.5 V, followed by regeneration of GeO_x from Ge and Li_2O at 1.18 V. Both cathodic and anodic curves overlap in the following CV scans, indicating high reversibility of Li_2O in the composite and good overall cycling stability.

Differential capacity analysis (d*Q*/d*V*) of the charge/discharge profiles of both the GeO_x/RGO composite and as-synthesized GeO_x was conducted to illustrate the difference in utilization of Li_2O for reversible Li storage between GeO_x/RGO and GeO_x. As indicated by the redox peaks at 0.50/1.12 V in **Figure 3**a–c, the reversible utilization of Li_2O can be realized in the composite at 0.1 C rate (Figure 3a) and even at higher rates of 1 C and 3 C (Figure 3b,c). The as-synthesized GeO_x shows comparatively high polarization, as indicated by the lower potential of the cathodic peak corresponding to formation of Li_2O. Furthermore, the intensities of redox peaks corresponding to utilization of Li_2O are lower at 0.1 C (Figure 3d), further diminished at 1 C (Figure 3e), and entirely gone at 3 C (Figure 3f), indicating

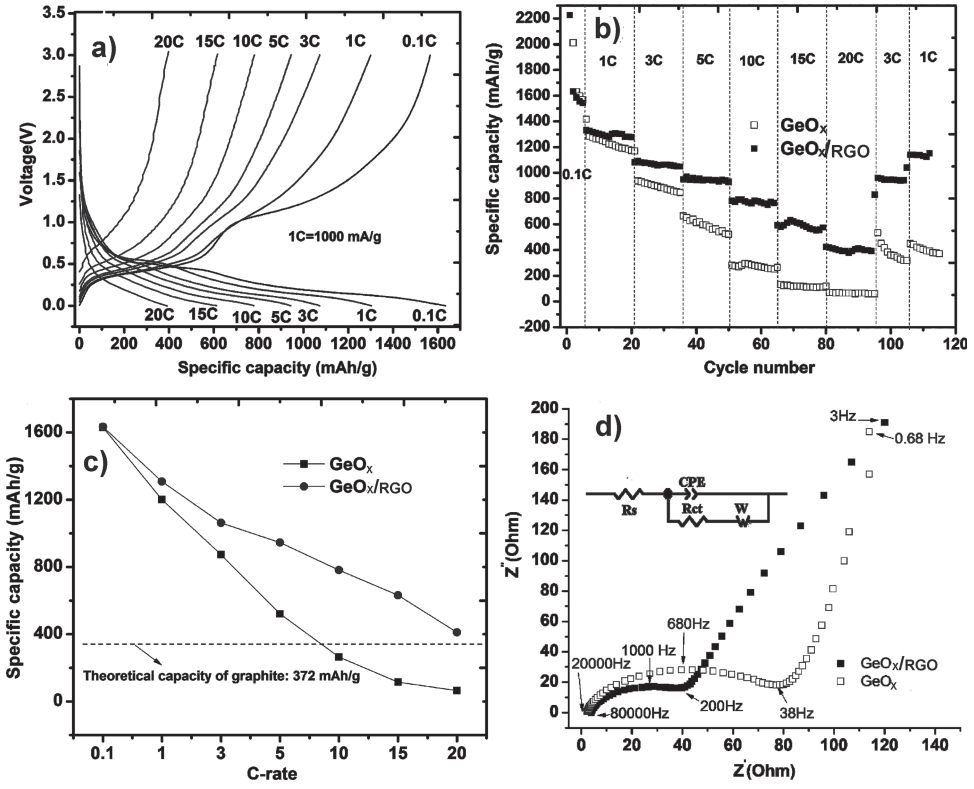

Figure 4. a) Typical charge/discharge curves (second cycles at each rate) of GeO_x/RGO at various C rates (1 C = 1000 mA g^{-1}); b) rate capability and cycling performance of GeO_x/RGO and GeO_x at various C rates; and comparison of c) rate performance and d) Nyquist plots of GeO_x/RGO and GeO_x (insert is the equivalent electrical circuit used for both spectra).

poor Li_2O utilization in the as-synthesized GeO_x. Successful utilization of Li_2O in GeO_x/RGO for reversible Li^+ storage may be attributed to the decreased barrier to both charge transfer and Li^+ diffusion in electrochemically formed Li_2O, due to the nanosized particles of GeO_x being in intimate contact with the conductive, well-dispersed RGO sheets. [25]

The rate capability and cycling stability of the GeO_x/RGO composite were evaluated by gradually increasing the current rate step-wise from 0.1 C to 20 C, and then returning back to 1 C. **Figure 4**a displays typical charge/discharge profiles of the composite at various rates. Increased polarization was observed with increasing current density, particularly with respect to the plateaus at 0.5 V during discharge and 1.1 V during charge that are related to the reversible reaction of Li_2O, as also observed in the dQ/dV analysis (Figure 3a–c). Despite this, the composite exhibits excellent rate capability compared with as-synthesized GeO_x, as shown in Figures 4b,c. For example, the composite achieved high capacities of 800, 700, and 500 mAh g^{-1} at current rates of 5 C, 10 C, and 15 C, respectively. A substantial capacity of 410 mAh g^{-1} (higher than the theoretical capacity of graphite, 372 mAh g^{-1}) was obtained even at a high rate of 20 C. In contrast, a low capacity of only 50 mAh g^{-1} was obtained from GeO_x at a rate of 20 C. The GeO_x exhibits similar capacities to the GeO_x/RGO at low rates of 0.1 C and 1 C, but much lower capacities at rates higher than 3 C. This is because as current density increases dramatically, electron transport becomes the limiting step in the lithiation/delithiation processes. Graphene sheets have been widely studied as conductive additives to improve conductivity of electrode materials for electrochemical energy storage.[7,14,25,26,28,29,31,34,37,45] Here, we use $NaBH_4$ as the reducing agent to obtain RGO in the composite, where the C/O ratio of RGO is in the range of 5–8 and the conductivity of such RGO is comparable to that of graphene sheets.[43,44] Thus, the increased electrical conductivity of the GeO_x/RGO composite can significantly improve the processes' kinetics and achieve higher capacity. Besides that, due to the nanoscale particle size of GeO_x and relatively high carbon content (8.5 wt%) and uniformly dispersed RGO in the composite (Figure 1g and Figure S3, Supporting Information), voids among the nanoparticles and layers of RGO are formed.[34,45,48] Such void space is available for penetration of electrolyte into the composite to promote fast Li^+ transport during the charge/discharge processes.[48] Thus, this particular aggregated porous structure actually enables the fast electrochemical reaction. This is supported by electrochemical impedance spectroscopy (EIS) and the Randles equivalent electrical circuit, corresponding to the spectra, show that the GeO_x/RGO composite has a much lower charge transfer resistance (33.6 Ω) than the GeO_x (64.6 Ω) (Figure 4d and Supporting Information, Table S2). Overall, the observed excellent rate capability of the GeO_x/RGO composite should be attributed to the well dispersed RGO sheets and intrinsic high electronic and ionic conductivity of Ge. Furthermore, it is interesting that the GeO_x exhibits different cycling stabilities with and without RGO sheets. As shown in Figure 4b,

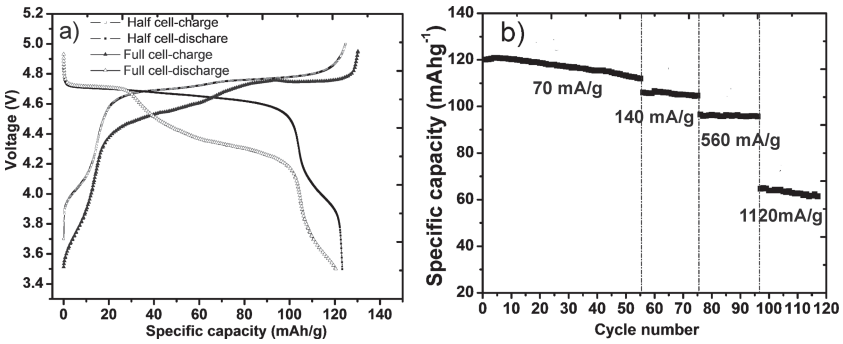

Figure 5. a) Typical charge/discharge curves of a Li-$LiNi_{0.5}Mn_{1.5}O_4$ half-cell and a GeO_x/RGO-$LiNi_{0.5}Mn_{1.5}O_4$ full cell; b) rate and cycling performance of the GeO_x/RGO-$LiNi_{0.5}Mn_{1.5}O_4$ full cell.

as the current rate was switched from 20 C to 3 C and/or 1 C, the capacity of the GeO_x/RGO was recovered and the cell continued its stable cycling, while low and continuously decreasing capacities were observed for the GeO_x. The poor capacity recovery of GeO_x is probably due to the pulverization of Ge particles induced by the unavoidable volume change during the Li^+ insertion/extraction processes, leading to loss of electrical contact.[5,9] The much improved cycling stability of GeO_x/RGO may be ascribed to the following factors. i) The flexible and well-dispersed RGO acts as a buffer layer, preventing aggregation of the GeO_x upon cycling, which enhances the electronic contact between the active materials and conductor (carbon black and RGO).[14,46] ii) GeO_x nanoparticles combined with amorphous structure can relieve the stress generated during alloying and de-alloying processes of Ge and consequently help avoid the pulverization.[17] iii) The formed Li_2O in the first discharge process partially remains among the Ge particles and may work as a buffer layer to accommodate volume expansion/contraction of Ge during the charge/discharge processes.[17,49]

To verify the composite's viability for practical application, the GeO_x/RGO composite anode was prelithiated and combined with a high voltage $LiNi_{0.5}Mn_{1.5}O_4$ cathode to construct a full Li-ion cell. **Figure 5**a shows typical charge/discharge profiles of both a half-cell of $LiNi_{0.5}Mn_{1.5}O_4$-Li and a full-cell of $LiNi_{0.5}Mn_{1.5}O_4$-GeO_x/RGO. In the half-cell, $LiNi_{0.5}Mn_{1.5}O_4$ exhibits a typical voltage profile of a high voltage spinel cathode and has a capacity of 125 mAh g^{-1} at a current density of 70 mA g^{-1}.[50] In the full-cell, a discharge capacity of 120 mAh g^{-1} (based on the cathode mass) is achieved. As shown in Figure 6a, the full cell has discharge plateaus at 4.7 and 4.3 V, and delivers an average discharge plateau of 4.4 V. The full cell also exhibits high capacity and good stability even when cycled at high current densities. As shown in Figure 5b, the cell delivered 100 mAh g^{-1} with 83% capacity retention when cycled at 560 mA g^{-1}, and can even be cycled at a current density of 1120 mA g^{-1} with a stable capacity of 65 mAh g^{-1}.

3. Conclusions

A GeO_x/reduced graphene oxide composite was successfully synthesized via a facile one-step reduction approach. The composite is composed of GeO_x ($1.01 < x < 1.07$) nanoparticles that are in intimate contact with well-dispersed RGO sheets. The XRD characterization indicates GeO_x in the composite is amorphous. The well-dispersed RGO sheets, nanosized particles, and amorphous phase greatly enhance electron transfer and lithiation/delithiation kinetics in the composite. When cycled at a low current density of 100 mA g^{-1}, the composite delivers a high reversible capacity of 1600 mAh g^{-1}, indicating the reversible utilization of Li_2O. At high current rates, the composite exhibits excellent rate capability. For example, a substantial capacity of 410 mAh g^{-1} was obtained even at a high rate of 20 C, which is higher than the theoretical capacity of graphite (372 mAh g^{-1}). The high reversible capacity and excellent rate capability of the composite are ascribed to the incorporation of conductive RGO sheets. Furthermore, the GeO_x/RGO composite was successfully utilized as an anode in combination with a high voltage $LiNi_{0.5}Mn_{1.5}O_4$ cathode to form a full cell, which showed promising performance as a high power Li-ion battery and demonstrated the feasibility of the composite for practical applications. The study indicates that a strategy of introducing a conductive reduced graphene oxide network into electrode materials presents an effective approach to enhance both the rate capability and cycling stability of high capacity germanium-based anode materials.

4. Experimental Section

Synthesis of GeO_x/RGO Composite: Graphene oxide (GO) was prepared from natural graphite by a modified Hummer's method,[39,51] and dispersed in water to form a GO dispersion (about 1 mg mL^{-1}). 0.01 g of PVP was then added into 50 mL of the above GO dispersion and dispersed by ultrasonication, obtaining GO/PVP dispersion for further use. The GeO_x/RGO composite was synthesized via a facile self-assembly approach by modifying the synthesis process of Ge nanoparticles.[52] The germanium-containing precursor was GeO_2. Typically, GeO_2 (1 g) was added in deionized (DI) water (10 mL). After adding NH_4OH solution (5 mL, 14.8 mol L^{-1}) into the above mixture, a clear and transparent solution was quickly obtained. The above solution was mixed with GO/PVP dispersion (50 mL) and further dispersed by probe ultrasonication. When the reducing agent, $NaBH_4$ solution (1.8 g $NaBH_4$ dissolved in 20 mL of DI water at 0 °C), was added drop-wise with magnetic stirring, the color of the dispersion changed from brown to black. With continued addition of the $NaBH_4$ solution, a suspension containing brownish-red particles was obtained. After 12 hours' magnetic stirring, the precipitate was centrifuged and washed three times with each of DI water and ethanol, and then dried at 60 °C under vacuum for 12 h. For comparison, the GeO_x without graphene was synthesized by a similar approach, simply excluding the addition of graphene oxide.

Characterization: The structure of the obtained samples was characterized on a Rigaku Dmax-2000 X-ray powder diffractometer using Cu Kα radiation (λ = 1.5418 Å). The operating voltage and current were kept at 40 kV and 30 mA, respectively. The XRD patterns were obtained with scan speed of 0.02° per step over a 2θ range of 10–80°. TEM images were taken on a JEOL 1200 microscope. TG-MS analysis was performed on a TA Instruments TGA 2050 with a Balzers ThermoStar 1–300 amu mass spectrometer at a heating speed of 10 °C min^{-1} under Ar flow. FTIR analysis was performed on a Hyperion 3000 FT-IR microscope.

Elemental contents of carbon and oxygen in the GeO_x/RGO composite were analyzed on a CE-440 Elemental Analyzer and PerkinElmer Model 240 Elemental Analyzer, respectively.

The electrochemical properties of the materials were evaluated using CR2016-type coin cells. For slurry preparation, GeO_x/RGO was first mixed with Super P carbon black and lithium polyacrylate (Li-PAA) binder with a weight ratio of 85:5:10. The slurry was then cast onto a copper foil current collector and dried at 60 °C for 3 h under vacuum. Electrodes with a diameter of 1.27 cm were punched from the dried slurry. Finally, coin cells were assembled in an argon-filled glovebox (MBraun, Inc.), each having a GeO_x/RGO electrode, lithium anode, Celgard 2400 polypropylene separator, and 1 m $LiPF_6$ in a mixture of ethylene carbonate, diethyl carbonate and dimethyl carbonate (EC:DEC:DMC, 2:1:2 by vol.) electrolyte. In the present work, a full cell was also constructed by combining a prelithiated GeO_x/RGO anode, $LiNi_{0.5}Mn_{1.5}O_4$ cathode, and the same electrolyte, and was tested electrochemically. The prelithiation of the GeO_x/RGO electrode was performed according to a previously reported method.[53] The electrochemical performance of the cells was evaluated by galvanostatic charge/discharge on an Arbin BT-2000 battery tester at room temperature under various current densities in voltage ranges of 0.01–3 V and 3.5–4.9 V for half-cells and full-cells, respectively. Cyclic voltammetry measurements were carried out on a CHI 660d potentiostat at a scan speed of 0.1 mV s^{-1} in the voltage range of 0.01–3 V, and electrochemical impedance spectrometry analysis was performed on the same instrument in a frequency range of 10^5–0.01 Hz.

Supporting Information

Supporting Information is available from the Wiley online Library or from the author.

Acknowledgements

The authors would like to acknowledge financial support from the U.S. Department of Energy's (DOE's) Office of Electricity Delivery and Energy Reliability (OE) (under Contract No. 57558). The authors are also grateful for beneficial discussions with Dr. Imre Gyuk of the DOE-OE Grid Storage Program.

Received: June 2, 2013
Revised: July 22, 2013
Published online: September 19, 2013

[1] M. Armand, J. M. Tarascon, *Nature* **2008**, *451*, 652.
[2] J. B. Goodenough, Y. Kim, *Chem. Mater.* **2010**, *22*, 587.
[3] S. Flandrois, B. Simon, *Carbon* **1999**, *37*, 165.
[4] C. K. Chan, H. Peng, G. Liu, K. McIlwrath, X. F. Zhang, R. A. Huggins, Y. Cui, *Nat. Nanotechnol.* **2008**, *3*, 31.
[5] G. L. Cui, L. Gu, L. J. Zhi, N. Kaskhedikar, P. A. van Aken, K. Mullen, J. Maier, *Adv. Mater.* **2008**, *20*, 3079.
[6] Y. Idota, T. Kubota, A. Matsufuji, Y. Maekawa, T. Miyasaka, *Science* **1997**, *276*, 1395.
[7] H. Wang, L.-F. Cui, Y. Yang, H. S. Casalongue, J. T. Robinson, Y. Liang, Y. Cui, H. Dai, *J. Am. Chem. Soc.* **2010**, *132*, 13978.
[8] C. S. Fuller, J. C. Severiens, *Phys. Rev.* **1954**, *96*, 21.
[9] C. K. Chan, X. F. Zhang, Y. Cui, *Nano Lett.* **2008**, *8*, 307.
[10] M. H. Seo, M. Park, K. T. Lee, K. Kim, J. Kim, J. Cho, *Energy Environ. Sci.* **2011**, *4*, 425.
[11] H. Lee, M. G. Kim, C. H. Choi, Y. K. Sun, C. S. Yoon, J. Cho, *J. Phys. Chem. B* **2005**, *109*, 20719.
[12] L. Baggetto, P. H. L. Notten, *J. Electrochem. Soc.* **2009**, *156*, A169.
[13] J. Z. Wang, N. Du, H. Zhang, J. X. Yu, D. R. Yang, *J. Mater. Chem.* **2012**, *22*, 1511.
[14] D. J. Xue, S. Xin, Y. Yan, K. C. Jiang, Y. X. Yin, Y. G. Guo, L. J. Wan, *J. Am. Chem. Soc.* **2012**, *134*, 2512.
[15] J. S. Cheng, J. Du, *CrystEngComm* **2012**, *14*, 397.
[16] K. H. Seng, M. H. Park, Z. P. Guo, H. K. Liu, J. Cho, *Angew. Chem. Int. Ed.* **2012**, *51*, 5657.
[17] X. L. Wang, W. Q. Han, H. Y. Chen, J. M. Bai, T. A. Tyson, X. Q. Yu, X. J. Wang, X. Q. Yang, *J. Am. Chem. Soc.* **2011**, *133*, 20692.
[18] J. K. Feng, M. O. Lai, L. Lu, *Electrochem. Commun.* **2011**, *13*, 287.
[19] R. Yi, J. Feng, D. Lv, M. L. Gordin, S. Chen, D. Choi, D. Wang, *Nano Energy* **2013**, *2*, 498.
[20] Y. Xia, Y. Xiong, B. Lim, S. E. Skrabalak, *Angew. Chem. Int. Ed.* **2009**, *48*, 60.
[21] H. Kim, J. Cho, *Nano Lett.* **2008**, *8*, 3688.
[22] R. Yi, F. Dai, M. L. Gordin, S. Chen, D. Wang, *Adv. Energy Mater.* **2013**, *3*, 295.
[23] A. K. Geim, K. S. Novoselov, *Nat. Mater.* **2007**, *6*, 183.
[24] X. Li, G. Zhang, X. Bai, X. Sun, X. Wang, E. Wang, H. Dai, *Nat. Nanotechnol.* **2008**, *3*, 538.
[25] D. Wang, D. Choi, J. Li, Z. Yang, Z. Nie, R. Kou, D. Hu, C. Wang, L. V. Saraf, J. Zhang, I. A. Aksay, J. Liu, *ACS Nano* **2009**, *3*, 907.
[26] Z.-S. Wu, W. Ren, L. Wen, L. Gao, J. Zhao, Z. Chen, G. Zhou, F. Li, H.-M. Cheng, *ACS Nano* **2010**, *4*, 3187.
[27] G. Zhou, D.-W. Wang, F. Li, L. Zhang, N. Li, Z.-S. Wu, L. Wen, G. Q. Lu, H.-M. Cheng, *Chem. Mater.* **2010**, *22*, 5306.
[28] S.-M. Paek, E. Yoo, I. Honma, *Nano Lett.* **2009**, *9*, 72.
[29] G. Wang, B. Wang, X. Wang, J. Park, S. Dou, H. Ahn, K. Kim, *J. Mater. Chem.* **2009**, *19*, 8378.
[30] S. Yang, X. Feng, K. Muellen, *Adv. Mater.* **2011**, *23*, 3575.
[31] B. Luo, B. Wang, X. Li, Y. Jia, M. Liang, L. Zhi, *Adv. Mater.* **2012**, *24*, 3538.
[32] J. K. Lee, K. B. Smith, C. M. Hayner, H. H. Kung, *Chem. Commun.* **2010**, *46*, 2025.
[33] J. Cheng, J. Du, *CrystEngComm* **2012**, *14*, 397.
[34] D. Wang, R. Kou, D. Choi, Z. Yang, Z. Nie, J. Li, L. V. Saraf, D. Hu, J. Zhang, G. L. Graff, J. Liu, M. A. Pope, I. A. Aksay, *ACS Nano* **2010**, *4*, 1587.
[35] S. Yang, X. Feng, S. Ivanovici, K. Muellen, *Angew. Chem. Int. Ed.* **2010**, *49*, 8408.
[36] P. Poizot, S. Laruelle, S. Grugeon, L. Dupont, J. M. Tarascon, *Nature* **2000**, *407*, 496.
[37] Z. Song, T. Xu, M. L. Gordin, Y.-B. Jiang, I.-T. Bae, Q. Xiao, H. Zhan, J. Liu, D. Wang, *Nano Lett.* **2012**, *12*, 2205.
[38] R. Kou, Y. Shao, D. Wang, M. H. Engelhard, J. H. Kwak, J. Wang, V. V. Viswanathan, C. Wang, Y. Lin, Y. Wang, I. A. Aksay, J. Liu, *Electrochem. Commun.* **2009**, *11*, 954.
[39] W. S. Hummers, R. E. Offeman, *J. Am. Chem. Soc.* **1958**, *80*, 1339.
[40] M. Zacharias, J. Blasing, M. Lohmann, J. Christen, *Thin Solid Films* **1996**, *278*, 32.
[41] Y. Batra, D. Kabiraj, S. Kumar, D. Kanjilal, *J. Phys. D: Appl. Phys.* **2007**, *40*, 4568.
[42] B. R. Taylor, S. M. Kauzlarich, H. W. H. Lee, G. R. Delgado, *Chem. Mater.* **1998**, *10*, 22.
[43] H.-J. Shin, K. K. Kim, A. Benayad, S.-M. Yoon, H. K. Park, I.-S. Jung, M. H. Jin, H.-K. Jeong, J. M. Kim, J.-Y. Choi, Y. H. Lee, *Adv. Funct. Mater.* **2009**, *19*, 1987.
[44] S. Pei, H.-M. Cheng, *Carbon* **2012**, *50*, 3210.
[45] N. Mahmood, C. Zhang, J. Jiang, F. Liu, Y. Hou, *Chem. Eur. J.* **2013**, *19*, 5183.
[46] S. Xin, Y.-G. Guo, L.-J. Wan, *Acc. Chem. Res.* **2012**, *45*, 1759.

[47] S. Yoon, C. M. Park, H. J. Sohn, *Electrochem. Solid State* **2008**, *11*, A42.
[48] N. Mahmood, C. Zhang, Y. Hou, *Small* **2013**, *9*, 1321.
[49] Z. Wen, S. Cui, H. Kim, S. Mao, K. Yu, G. Lu, H. Pu, O. Mao, J. Chen, *J. Mater. Chem.* **2012**, *22*, 3300.
[50] J. H. Kim, S. T. Myung, Y. K. Sun, *Electrochim. Acta* **2004**, *49*, 219.
[51] N. I. Kovtyukhova, P. J. Ollivier, B. R. Martin, T. E. Mallouk, S. A. Chizhik, E. V. Buzaneva, A. D. Gorchinskiy, *Chem. Mater.* **1999**, *11*, 771.
[52] J. Wu, Y. Sun, R. Zou, G. Song, Z. Chen, C. Wang, J. Hu, *CrystEngComm* **2011**, *13*, 3674.
[53] G. Derrien, J. Hassoun, S. Panero, B. Scrosati, *Adv. Mater.* **2007**, *19*, 2336.